Journal of Environmental Management 317 (2022) 115425

Contents lists available at ScienceDirect

Journal of Environmental Management

journal homepage: www.elsevier.com/locate/jenvman

Research article

Photooxidation of Fe(II) to schwertmannite promotes As(III) oxidation and immobilization on pyrite under acidic conditions

Lihu Liu [a], Diman Guo [a], Guohong Qiu [a], Chengshuai Liu [b], Zengping Ning [b,*]

[a] Key Laboratory of Arable Land Conservation (Middle and Lower Reaches of Yangtse River), Ministry of Agriculture and Rural Affairs, Hubei Key Laboratory of Soil Environment and Pollution Remediation, College of Resources and Environment, Interdisciplinary Sciences Research Institute, Huazhong Agricultural University, Wuhan, 430070, Hubei Province, China

[b] State Key Laboratory of Environmental Geochemistry, Institute of Geochemistry, Chinese Academy of Sciences, Guiyang, 550081, Guizhou Province, China

ARTICLE INFO

Keywords:
Sulfide mineral
Reactive oxygen species
Arsenic
AMD
Sunlight
Schwertmannite

ABSTRACT

Pollution of arsenic (As) in acid mine drainage (AMD) is a universal environmental problem. The weathering of pyrite (FeS_2) and other sulfide minerals leads to the generation of AMD and accelerates the leaching of As from sulfide minerals. Pyrite can undergo adsorption and redox reactions with As, affecting the existing form and biotoxicity of As. However, the interaction process between As and pyrite in AMD under sunlight radiation remains unclear. Here, we found that the oxidation and immobilization of arsenite (As(III)) on pyrite can be obviously promoted by the reactive oxygen species (ROS) in sunlit AMD, particularly by •OH. The reactions between hole-electron pairs and water/oxygen adsorbed on excited pyrite resulted in the production of H_2O_2, •OH and $O_2^{\bullet-}$, and •OH was also generated through the photo-Fenton reaction of Fe^{2+}/$FeOH^{2+}$. Weakly crystalline schwertmannite formed from the oxidation of Fe^{2+} ions by •OH contributed much to the adsorption and immobilization of As. In the mixed system of pyrite (0.75 g L^{-1}), Fe^{2+} (56.08 mg L^{-1}) and As(III) (1.0 mg L^{-1}) at initial pH 3.0, the decrease ratio of dissolved total As concentration was 1.6% under dark conditions, while it significantly increased to 69.0% under sunlight radiation. The existence of oxygen or increase in initial pH from 2.0 to 4.0 accelerated As(III) oxidation and immobilization due to the oxidation of more Fe^{2+} and production of more ROS. The present work shows that sunlight significantly affects the transformation and migration of As in AMD, and provides new insights into the environmental behaviors of As.

1. Introduction

Mining and smelting activities for energy and material needs have caused global environmental problems (Aydin, 2014; Aydin et al., 2012; Köne and Büke, 2010). As reported, there are hundreds of thousands of abandoned mines worldwide, many of which have been producing acid mine drainage (AMD) in the past few decades (Tabelin et al., 2020). AMD can cause secondary pollution to groundwater, surrounding rivers and soils (Liu et al., 2021; Tabelin et al., 2020). Arsenic (As) is a highly toxic metalloid widely present in nature, and can cause harm to humans even at extremely low levels (μg L^{-1}) due to its chronic toxicity (Ahmad et al., 2020; Koley, 2021; Xu et al., 2021). Some serious health problems, such as skin, blood vessel and nervous system dysfunctions, and even skin, kidney and liver cancers are associated with the long-term intake of As-contaminated water or food (Podgorski and Berg, 2020; Zhong et al., 2020). Arsenic can occur in more than 300 minerals, generally with contents below 1 mg kg^{-1} in nature. However, the content of As can be very high in many sulfide minerals related to gold and copper ore, including tennantite ($Cu_{12}As_4S_{13}$), enargite (Cu_3AsS_4) and arsenopyrite (FeAsS) (Hong et al., 2018, 2021). The weathering of such sulfide minerals rich in As by water, oxygen and microorganism will generate AMD with high concentrations of As, impacting the aquatic environment. Thus, the environmental behaviors of As in AMD systems have attracted great attention in recent years (Alonso et al., 2020; Asif et al., 2021; Gabarron et al., 2018; Park et al., 2021).

As the most abundant sulfide mineral in the nature, pyrite (FeS_2) is commonly found in metal sulfide mines and coal mines (Tabelin et al., 2020). Pyrite is often separated and abandoned as tailings from other metallic sulfide ores (such as gold and copper ore) owing to its low economic value (Han et al., 2020; Zhang et al., 2021). In supergene environments, pyrite can be rapidly oxidized after contact with air, water and microorganism (Diao et al., 2013). The release of sulfuric acid

* Corresponding author.
E-mail address: ningzengping@mail.gyig.ac.cn (Z. Ning).

https://doi.org/10.1016/j.jenvman.2022.115425
Received 6 February 2022; Received in revised form 17 May 2022; Accepted 25 May 2022
Available online 7 June 2022

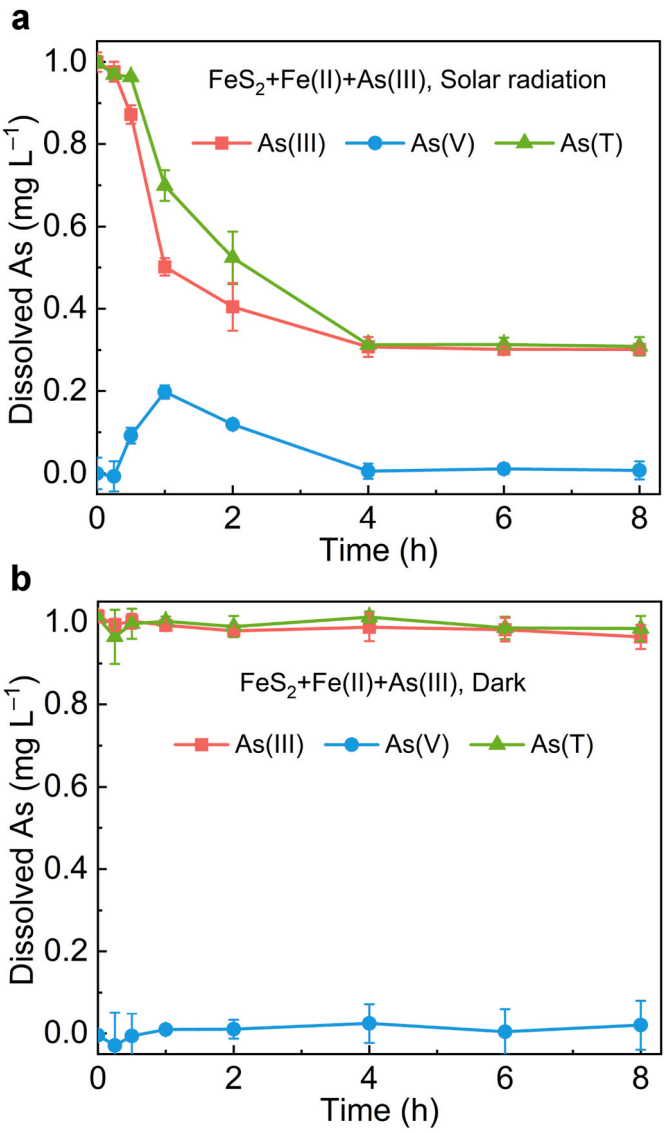

Fig. 1. Dissolved As species in the system of pyrite + Fe^{2+} + As(III) under sunlight radiation (a) and dark (b) in air at initial pH 3.0. Initial concentration: $[pyrite]_0 = 0.75$ g L^{-1}, $[Fe^{2+}]_0 = 56.08$ mg L^{-1} and $[As(III)]_0 = 1.0$ mg L^{-1}.

during pyrite oxidation can not only lead to the formation of AMD, but also aggravate the leaching of As and other metals from sulfide minerals (Diao et al., 2013; Ferreira et al., 2021). The biotoxicity and migration ability of As in environments are highly dependent on its species. For soluble inorganic As, trivalent As (arsenite, As(III)) has stronger toxicity and migration ability than pentavalent As (arsenate, As(V)) (Ding et al., 2018; Liu et al., 2020). As(III) is the major As species released from the weathering of As-bearing sulfide minerals in natural environments (Hong et al., 2021; Yu et al., 2007). Overall, the pollution of As(III) in water and soil caused by mining, flotation and smelting of metallic sulfide ores has become a common environmental problem in the world (Tabelin et al., 2020; Zhang et al., 2021).

Many previous studies have been focused on the adsorption, co-precipitation and redox processes of As(III) on pyrite, and confirmed that pyrite greatly affects the fate of As in the mining environment (Fu et al., 2021; Le Pape et al., 2017; Qiu et al., 2018). The sunlight that radiates the Earth's surface involves UV-B (280–315 nm), UV-A (315–400 nm) and visible light (Hong et al., 2018). In natural AMD environments, sunlight participates in the geochemical cycling of some toxic elements (Doane, 2017). Recently, increasing attention has been paid to the ROS generation induced by sunlight radiation on natural semiconductor minerals, its subsequent influence on the generation of secondary minerals and the fate of coexisting contaminants (Doane, 2017; Georgiou et al., 2015; Lu et al., 2019). For example, sunlight radiation can catalyze ferrihydrite and goethite to oxidize As(III) (Bhandari et al., 2011, 2012), and also induce the production of ROS on antimony trioxide and arsenopyrite, accelerating the oxidation of these minerals and the leaching of Sb and As (Hong et al., 2018; Hu et al., 2014). Under sunlight radiation, the main iron oxides generated from the transformation of ferrihydrite induced by Fe(II) also significantly differ from those produced in the dark (Shu et al., 2019). Pyrite is a semiconductor mineral that may produce •OH and $O_2^{\bullet-}$ under light radiation (Eqs. 25–27 in Table S1) (Hu et al., 2014; Kong et al., 2015; Shu et al., 2019), which can oxidize coexisting As(III). Therefore, clarifying the effect of sunlight radiation on the adsorption and oxidation of As(III) on the surface of pyrite under acidic conditions may improve the understanding of the fate of As in AMD environments.

In our previous work, sunlight radiation was found to enhance the generation of ROS on pyrite and subsequent oxidation of As(III) in circumneutral environments (Liu et al., 2021). The photooxidation and adsorption of pyrite for As(III) in AMD may be significantly different from those in circumneutral environments. There is also a large amount of dissolved Fe^{2+} in AMD, and $O_2^{\bullet-}$ formed in the oxidation process of Fe^{2+} by oxygen may further oxidize As(III) (Eqs. 8 and 18 in Table S1) (Kong et al., 2015). In addition, the oxidation products of Fe^{2+} by oxygen and ROS significantly vary with pH and coexisting anion, which could directly affect the adsorption of As. For example, schwertmannite is formed at pH 3.0, and goethite and lepidocrocite are generated with increasing pH to 6.0 during the oxidation of Fe^{2+} by the ROS formed on ferrihydrite under sunlight radiation (Shu et al., 2019). However, little is known about the interaction process between As and pyrite in AMD under sunlight radiation.

In this work, the reaction process between As(III) and pyrite under acidic conditions was investigated with outdoor sunlight radiation. Subsequently, ultraviolet (UV) radiation was used in the laboratory to qualitatively and quantitatively analyze the intermediate products, possible ROS and their influence on the oxidation and migration of As (III). The study aims to clarify the effect and underlying mechanism of sunlight on the interaction of pyrite and As(III) in AMD environments.

2. Materials and methods

2.1. Minerals

Pyrite was mined at Shangbao Village, Hunan Province, China, ground and sieved (75 μm). The detailed cleaning, drying and analysis of the chemical composition are shown in the Supporting Information. The relative contents of Fe and S were 43.0 wt% and 55.7 wt%, respectively.

2.2. Photochemical oxidation of As(III)

Fig. S1 shows the flowchart of the experiments in this work. As_2O_3 was dissolved with NaOH solution to prepare 1000 mg L^{-1} As(III) stock solution. Then, the stock solution was diluted, and $FeSO_4$ was added after adjustment of the initial pH to 3.0 with H_2SO_4. The final concentrations of As(III) and Fe^{2+} were 1.0 and 56.08 mg L^{-1}, respectively. The photochemical reaction was carried out in a quartz tube with magnetic stirring under radiation by sunlight or UV light in air. Each quartz tube contained 0.075 g of pyrite powder and 100 mL of acidic As(III)-containing solution. The experiment under sunlight radiation was conducted from 09:00 to 17:00 on June 30, 2021, with the air temperature ranging from 26 °C to 35 °C. The highest light intensity was 2.7 and 65.7 mW cm^{-2} within the wavelength of 320–400 and 400–1000 nm at 12:30, respectively. A Precise photochemical instrument (PL-03) equipped with a mercury lamp was applied to conduct the experiments under UV radiation. The highest light intensity within 365–400 nm was 2.5 mW cm^{-2}, and a filter was equiped to remove the visible light.

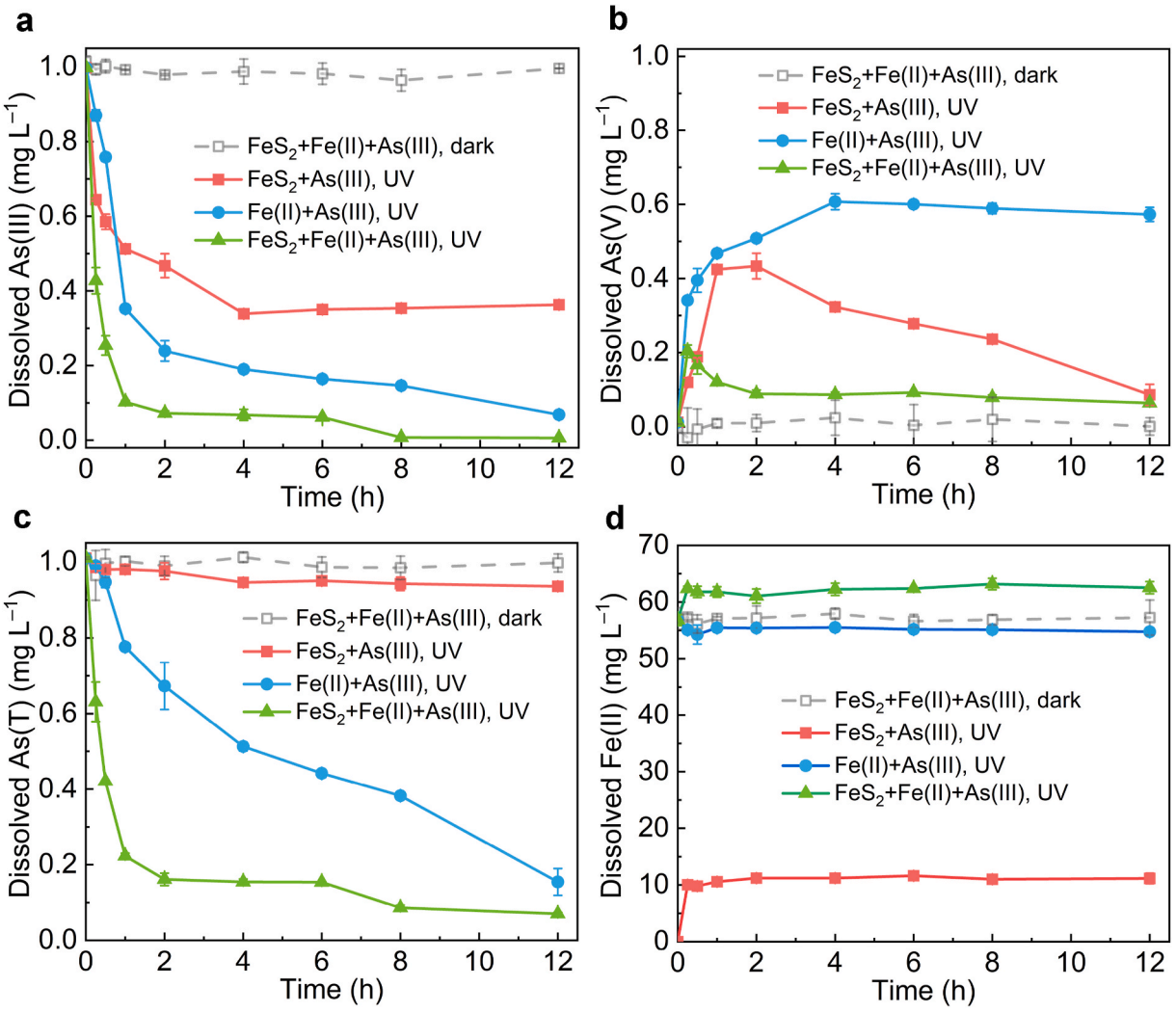

Fig. 2. Dissolved As(III) (a), As(V) (b), As(T) (c) and Fe(II) (d) in different reactions in air at initial pH 3.0. Initial concentration: $[\text{pyrite}]_0 = 0.75$ g L^{-1}, $[Fe^{2+}]_0 = 56.08$ mg L^{-1} and $[\text{As(III)}]_0 = 1.0$ mg L^{-1}.

Suspension (3 mL) was taken out after different time of reaction. The solution was collected after filtration by a millipore filter, and the remaining solid products were collected after rinsing with deoxygenated deionized water and freeze-drying.

The role of dissolved oxygen was investigated by respectively introducing nitrogen and oxygen into the reaction system at pH 3.0. During the experiment in nitrogen, high-purity nitrogen (99.999%) was continuously introduced into the solution from 0.5 h before the beginning to the end of the reaction to remove dissolved oxygen. The effect of pH (2.0, 3.0 and 4.0) was studied in the reaction system in air. The tested reaction systems included those consisting of single As(III) and pyrite, and mixture of pyrite and As(III) (pyrite + As(III)), $FeSO_4$ and As(III) ($FeSO_4$ + As(III)), and pyrite, $FeSO_4$ and As(III) (pyrite + $FeSO_4$ + As(III)).

2.3. Analysis methods

The analyses of crystalline phase, surface characteristics and structure of solids were conducted with X-ray diffraction (XRD) patterns recorded on a Shimadzu diffractometer (6100), scanning electron microscopy (SEM) images taken on a Hitachi microscope (SU8000), Fourier transform infrared spectroscopy (FTIR) spectra collected on a Bruker spectrometer (VERTEX 70), X-ray photoelectron spectroscopy (XPS) spectra obtained on a Thermo spectrometer (VG Multilab 2000) and X-ray absorption fine structure (XAFS) spectra tested at the 1W1B beamline in Beijing Synchrotron Radiation Facility (BSRF). The characterization details are shown in the Supporting Information. The determination of dissolved As concentration was conducted on an atomic fluorescence spectrometer (AFS-8530, Haiguang, China) (Liu et al., 2019). A UV–visible spectrophotometer (UV-1800, Mapada) was employed to analyze the concentration of dissolved Fe with *o*-phenanthroline as the developer at 510 nm (Tamura et al., 1974). More details about the determination of As and Fe concentration are presented in the Supporting Information. $OH^{\bullet}$, $O_2^{\bullet-}$ and $Fe^{2/3+}$ were trapped by 200 mmol L^{-1} t-butanol (TBA), 25 mg L^{-1} superoxide dismutase (SOD) and 1.0 mmol L^{-1} KH_2PO_4, respectively, so as to study their roles in As(III) photooxidation (Hong et al., 2018, 2020). Quantitative determination of cumulative •OH in the photochemical system was conducted on a high-performance liquid chromatograph (1260 Infinity, Agilent) after 10 mmol L^{-1} sodium benzoate (BA) was added (Joo et al., 2005). A UV–visible spectrophotometer was used to quantitatively measure H_2O_2 with the *N,N*-diethyl-*p*-phenylenediamine (DPD) method (Lee and Choi, 2002).

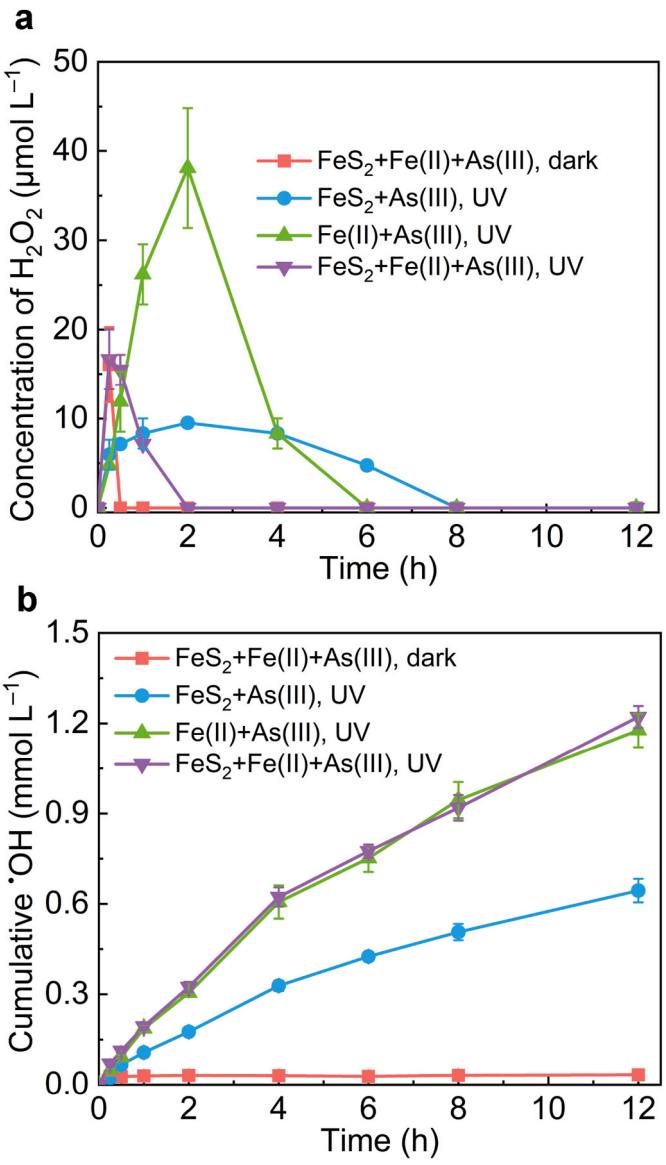

Fig. 3. Instantaneous concentrations of H_2O_2 (a) and cumulative concentrations of •OH (b) in different reactions in air at initial pH 3.0. Initial concentration: $[pyrite]_0$ = 0.75 g L^{-1}, $[Fe^{2+}]_0$ = 56.08 mg L^{-1} and $[As(III)]_0$ = 1.0 mg L^{-1}.

3. Results

3.1. Photochemical reactions between pyrite and As(III)

The system of pyrite + $FeSO_4$ + As(III) at initial pH 3.0 was exposed to sunlight for 8 h (Fig. 1). There was an obvious decrease in the concentration of dissolved As(III) and total As (As(T)) while a first increase and then decrease in that of As(V) with reaction, and equilibrium occurred at about 4 h at dissolved As(T), As(V) and As(III) concentration of 0.31, 0.01 and 0.30 mg L^{-1}, respectively. The concentrations of various As species exhibited no significant change in the dark. The results suggested that sunlight radiation may remarkably accelerate As(III) oxidation and immobilization on pyrite in AMD.

Different reaction systems at initial pH 3.0 were exposed to UV radiation in the laboratory to examine the mechanism and the influencing factors of As(III) oxidation and immobilization. Under UV radiation, in the systems of pyrite + As(III), $FeSO_4$ + As(III) and pyrite + $FeSO_4$ + As (III), dissolved As(III) and As(T) concentration decreased, while dissolved As(V) concentration first increased and then decreased (Fig. 2a–c). In the above reaction systems, the final concentration of dissolved As(III) was 0.36, 0.07 and 0.01 mg L^{-1}, and that of dissolved As(T) was 0.93, 0.16 and 0.07 mg L^{-1}, respectively. In the single As(III) system, about 3% of As(III) was oxidized under UV radiation (Fig. S2). In the system of pyrite + As(III), about 2% As(III) was oxidized, and the As (T) concentration showed no obvious change in the dark (Fig. S3). These results further confirmed that light radiation enhanced As(III) oxidation and immobilization in the presence of pyrite under acidic conditions.

The concentration of dissolved Fe^{2+} was also determined in different reaction systems (Fig. 2d). Under UV radiation, the final concentration of dissolved Fe^{2+} was 11.15, 54.76 and 62.54 mg L^{-1} in the systems of pyrite + As(III), $FeSO_4$ + As(III) and pyrite + $FeSO_4$ + As(III), respectively. In the dark, the final concentration of dissolved Fe^{2+} was 8.02 and 57.27 mg L^{-1} in the systems of pyrite + As(III) and pyrite + $FeSO_4$ + As(III), respectively. These results indicated that UV radiation accelerated the release of Fe^{2+} from pyrite.

Fig. 3 shows the levels of instantaneous H_2O_2 and cumulative •OH in different reaction systems. In the reaction systems of pyrite + As(III), $FeSO_4$ + As(III) and pyrite + $FeSO_4$ + As(III) under UV radiation, the maximum instantaneous H_2O_2 content was 9.52, 38.10 and 16.67 μmol L^{-1}, and correspondingly the cumulative •OH content finally reached 0.64, 1.18 and 1.22 mmol L^{-1}, respectively. In the system of pyrite + $FeSO_4$ + As(III) in the dark, the maximum instantaneous H_2O_2 and cumulative •OH content was 16.07 and 33.00 μmol L^{-1}, respectively. These results suggested that in the system of pyrite + $FeSO_4$ + As(III), the production of H_2O_2 and •OH was promoted by UV radiation.

XRD and FTIR analyses of the solid products indicated that the crystalline phase of pyrite showed no change and no other mineral was generated under UV radiation and dark (Fig. S4). The characteristic band of pyrite is located at 418 cm^{-1}; that of SO_4^{2-} is located at 610, 1081, 1132 and 1185 cm^{-1}; that of adsorbed water is at 1633 and 3421 cm^{-1}; and that of As(V)–O–Fe occurs at 830 cm^{-1}, which may be due to the adsorption of As on the solid products or the production of iron arsenate after UV radiation (Majzlan et al., 2011; Qiu et al., 2018). Fe K-edge XAFS spectra were used to further analyze the composition of the solid products (Fig. 4a and Table S2). After 12 h of reaction in the dark, the pyrite crystal structure showed no significant change, while a small amount of schwertmannite ($Fe_8O_8(OH)_{8-2x}(SO_4)_x$, $1 < x < 1.75$) was formed under UV radiation.

XPS spectra were employed to analyze the surface species of As, Fe and S on pyrite after reaction under UV radiation and dark (Fig. 4b–d and Table S3). In the As $3d_{(5/2)}$ spectra, the main peaks of As(As(V)–O) and As (As(III)–O) have binding energies of 45.20 and 44.50 eV, respectively (Kim and Batchelor, 2009). No signal of As was observed after reaction in the dark; while after UV radiation, As was detected in the forms of As(As(V)–O) and As (As(III)–O) with the contents of 92.2% and 8.8%, respectively, further indicating that light radiation accelerates As(III) oxidation and immobilization. The signals occurring within 710.4–713.5, 708.7–711.7 and 706.2–707.8 eV in the Fe $2p_{(3/2)}$ spectra belong to the binding energies of Fe (Fe(III)–O), Fe (Fe(III)–S) and Fe (Fe (II)–S), respectively (Qiu et al., 2017). The relative content of Fe (Fe(II)–S) decreased from 71.0% to 66.3% and 62.6%, that of Fe (Fe(III)–S) increased from 23.3% to 28.1% and 28.6%, and that of Fe (Fe(III)–O) varied from 5.7% to 5.6% and 8.8% after reaction under dark and UV radiation, respectively. In the S $2p_{(3/2)}$ spectra, 161.49, 162.29, 162.82, 164.16 and 168.86 eV are associated with the binding energies of $S(S^{2-})$, $S(S_2^{2-}$-surface), $S(S_2^{2-}$-bulk), $S(S^0/S_n^{2-})$ and $S(SO_4^{2-})$, respectively (Chandra and Gerson, 2011; Wang et al., 2020). Compared with dark conditions, UV radiation led to no obvious change in the relative content of $S(S^{2-})$, $S(S_2^{2-}$-bulk) and $S(S^0/S_n^{2-})$, and slightly decreased and increased that of $S(S_2^{2-}$-surface) and $S(SO_4^{2-})$, respectively. Compared with pristine pyrite, the decrease in the relative content of $S(SO_4^{2-})$ under UV radiation and dark may be ascribed to the dissolution of pyrite surface. The SEM images also suggested a significant decrease in the particle size of pyrite under UV radiation and dark (Fig. S5).

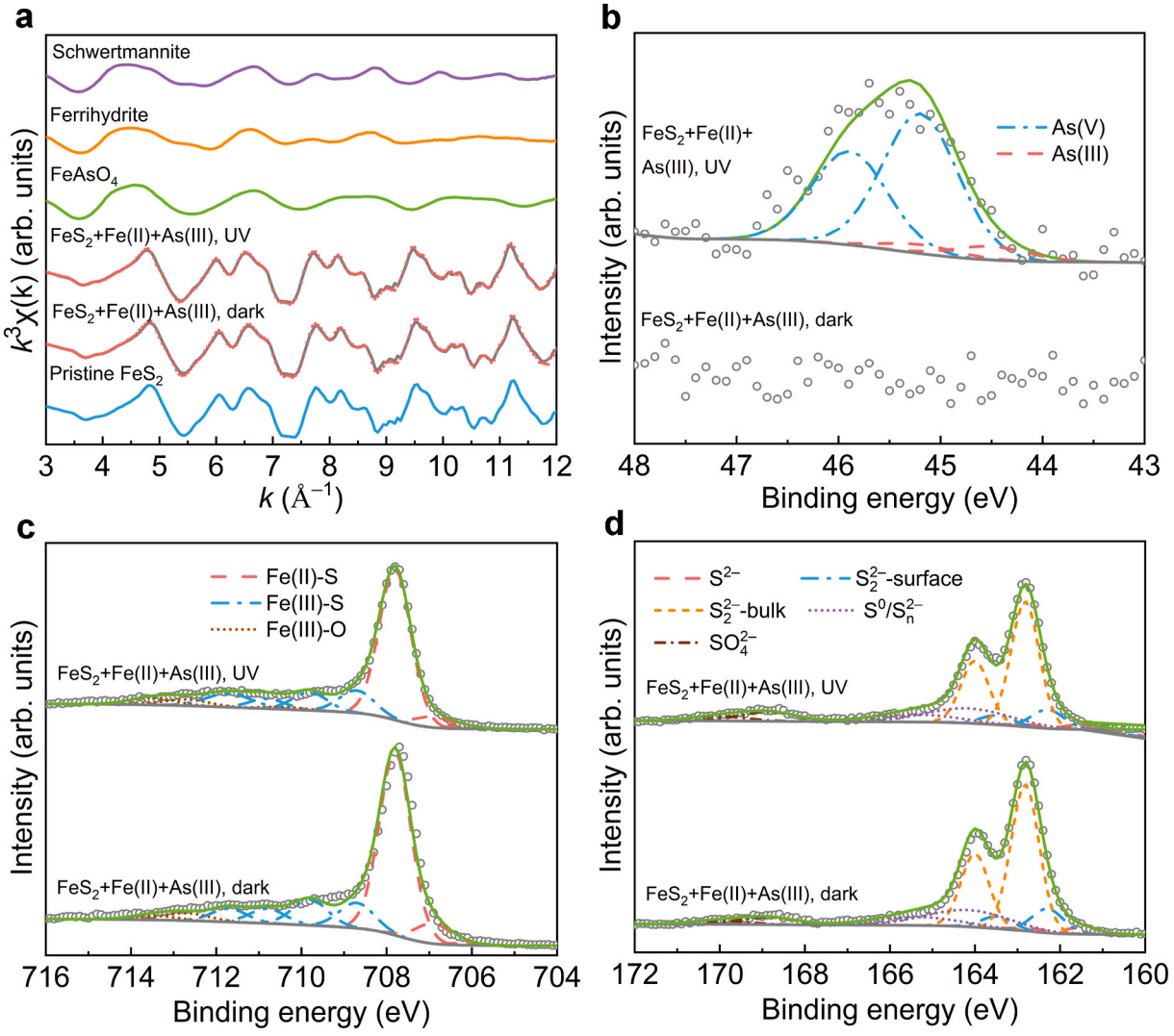

Fig. 4. Linear-combination fit (gray solid lines) of Fe K-edge EXAFS spectra (red dotted lines) (a), and deconvoluted XPS peaks of As $3d_{(5/2)}$ (b), Fe $2p_{(3/2)}$ (c) and S $2p_{(3/2)}$ (d) of pyrite after 12 h of reaction in the system of pyrite, Fe^{2+} and As(III) in air at initial pH 3.0. Initial concentration: $[pyrite]_0 = 0.75$ g L^{-1}, $[Fe^{2+}]_0 = 56.08$ mg L^{-1} and $[As(III)]_0 = 1.0$ mg L^{-1}. (For interpretation of the references to colour in this figure legend, the reader is referred to the Web version of this article.)

3.2. Influence of dissolved oxygen and pH

The photochemical reaction of pyrite, $FeSO_4$ and As(III) was also conducted respectively in nitrogen and oxygen to estimate the effect of dissolved oxygen (Fig. 5a and b). Dissolved As(III) concentration slowly decreased with reaction and reached 0.46 mg L^{-1} at 12 h in nitrogen, while it remarkably decreased in the first 1 h, followed by gradual decreases to 0 at 8 h in air, and rapidly decreased to 0 at 1 h in oxygen. The dissolved As(T) concentration exhibited no significant change in nitrogen, but remarkably decreased to 0.07 and 0 mg L^{-1} at 12 h in air and oxygen, respectively. The dissolved As(V) concentration continuously increased to 0.55 mg L^{-1} in nitrogen, and first increased and then decreased to 0.06 and 0 mg L^{-1} at 12 h in air and oxygen, respectively (Fig. S6). These results suggested that dissolved oxygen significantly promotes As(III) oxidation and immobilization.

The photochemical reaction of pyrite, $FeSO_4$ and As(III) at initial pH 2.0 and 4.0 was also performed to examine the influence of pH (Fig. 5c and d and Fig. S7), and the fluctuation of pH was less than 0.05. An increase in initial pH resulted in the reduction of As concentration. At initial pH 2.0, 3.0 and 4.0, the final dissolved As(III) concentration reached 0.38, 0 and 0 mg L^{-1}, and dissolved As(T) concentration was 0.99, 0.07 and 0 mg L^{-1}, respectively. Fig. S8 shows the corresponding dissolved $Fe^{2/3+}$ concentrations in these reaction systems. With increasing initial pH, the dissolved Fe^{2+} concentration showed little change, while the dissolved Fe^{3+} concentration exhibited an obvious decrease. These results implied that an increase in initial pH can accelerate As(III) oxidation and immobilization.

4. Discussion

4.1. Mechanism of photooxidation and immobilization of As(III)

Only 3% of As(III) was oxidized in the single As(III) system under UV radiation; and As(III) oxidation significantly increased without obvious immobilization of As in the system of pyrite + As(III); while As(III) oxidation and immobilization showed obvious increases in the system of $FeSO_4$ + As(III). These results demonstrate that pyrite promotes the oxidation of As(III), and the coexisting $FeSO_4$ enhances both the oxidation of As(III) and the immobilization of As(T) under light radiation. In the dark, the oxidation of water at sulfur defect sites and the reduction of oxygen on pyrite resulted in the generation of •OH and H_2O_2 (Zhang et al., 2016). Under light radiation, h^+_{vb}–e^-_{cb} pairs were generated on excited pyrite (Eq. 25 in Table S1) (Kong et al., 2015), which can interact with adsorbed water and oxygen to result in the

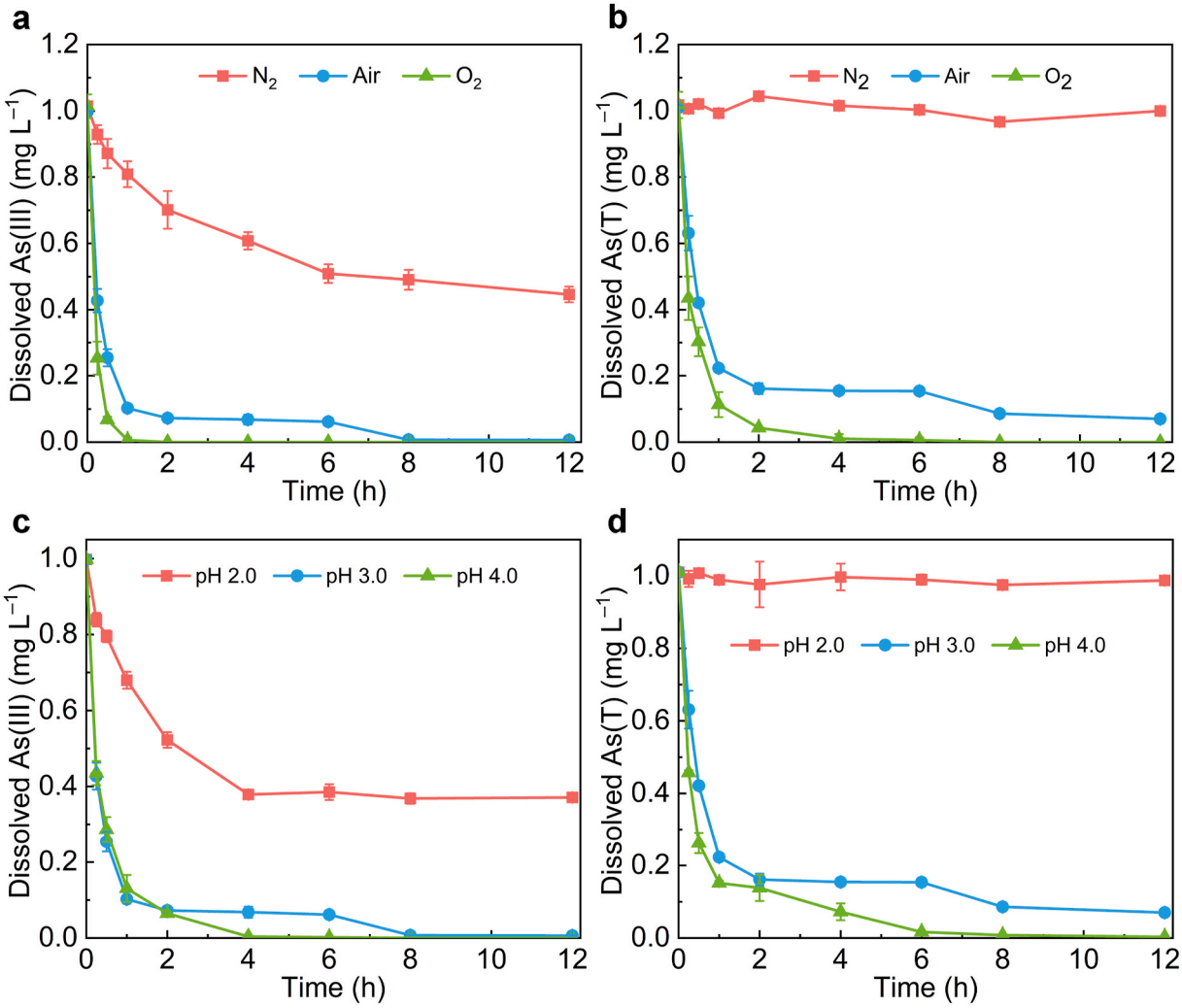

Fig. 5. Effects of dissolved oxygen (a, b) and initial pH (c, d) on dissolved As(III) and As(T) concentrations in the system of pyrite, Fe^{2+} and As(III) under UV radiation. Initial concentration: $[pyrite]_0 = 0.75\ g\ L^{-1}$, $[Fe^{2+}]_0 = 56.08\ mg\ L^{-1}$ and $[As(III)]_0 = 1.0\ mg\ L^{-1}$.

production of •OH and $O_2^{\bullet -}$ (Eqs. 26 and 27 in Table S1) (Hu et al., 2014; Shu et al., 2019). In addition, the release of Fe^{2+} from pyrite increased along with As(III) oxidation under light radiation (Fig. 2d), suggesting that light radiation promotes pyrite oxidative dissolution. The oxidation of Fe^{2+} to Fe^{3+} in the solution can promote $O_2^{\bullet -}$ generation (Eq. 18 in Table S1), and $Fe^{2+}/Fe(OH)^{2+}$ in the solution can undergo photo-Fenton reaction to form •OH under acidic conditions (Eqs. 22–24 in Table S1) (Hong et al., 2018). The formation of ROS such as •OH and $O_2^{\bullet -}$ on pyrite promoted As(III) oxidation (Eqs. 7–10 in Table S1). TBA, SOD and KH_2PO_4 were used to trap •OH, $O_2^{\bullet -}$ and $Fe^{2/3+}$ in the reaction system of pyrite + As(III) to examine the formation pathway and function of these ROS (Fig. 6a and b). As(III) oxidation was obviously inhibited by TBA and KH_2PO_4, while showed no obvious change when SOD was added, indicating that •OH generated from the photo-Fenton reaction of $Fe^{2+}/Fe(OH)^{2+}$ contributes greatly to As(III) oxidation.

The oxidation of $FeSO_4$ accelerated As(III) oxidation and immobilization. $Fe^{2/3+}$ and SO_4^{2-} exist in large amounts in AMD (Liu et al., 2018). The ROS formed from the photo-Fenton reaction of $Fe^{2+}/Fe(OH)^{2+}$ and the oxidation of Fe^{2+} promoted As(III) oxidation (Eqs. 7–10, 18–24 in Table S1). TBA, SOD and KH_2PO_4 were used to trap •OH, $O_2^{\bullet -}$ and $Fe^{2/3+}$ in the system of pyrite + As(III) to elucidate the role and function of Fe^{2+} (Fig. 6c and d). TBA and KH_2PO_4 obviously decreased As(III) oxidation, and SOD slightly reduced As(III) oxidation. These results confirm that •OH generated from the photo-Fenton reaction of $Fe^{2+}/Fe(OH)^{2+}$ drives As(III) oxidation, which was further verified by the experimental results of the system of pyrite + $FeSO_4$ + As(III) in the presence of TBA, SOD and KH_2PO_4 (Fig. 6e and f). In the presence of $FeSO_4$, As immobilization was significantly promoted, indicating that the formation of schwertmannite from $FeSO_4$ oxidation leads to the immobilization of As(T). Schwertmannite ($Fe_8O_8(OH)_{8-2x}(SO_4)_x$, $1 < x < 1.75$), with a high affinity for As, is a weakly crystalline ferric oxyhydroxy-sulfate mineral preferentially formed through Fe^{2+} oxidation or Fe^{3+} hydrolysis in AMD (Liu et al., 2018). AsO_4^{3-} has a similar ion radius to SO_4^{2-} and strong complexation ability with Fe(III), and as a result, SO_4^{2-} in the tunnel structure of schwertmannite can be replaced by AsO_4^{3-} under AMD conditions (Wang et al., 2021). In our previous work, schwertmannite formation was also observed in the oxidation of $FeSO_4$ in ferrihydrite suspension and nitrate-containing solutions at pH 3.0 and 4.5 under light radiation (Liu et al., 2018; Shu et al., 2019). In this work, the •OH generated from the photo-Fenton reaction of $Fe^{2+}/Fe(OH)^{2+}$ contributed much to the oxidation of $FeSO_4$ to form schwertmannite.

Fig. 7 shows the possible oxidation and immobilization mechanism of As(III) on pyrite in AMD. Under sunlight radiation, $O_2^{\bullet -}$, •OH and H_2O_2 are produced through the reaction of h_{vb}^+–e_{cb}^- pairs with water and oxygen on pyrite. At the same time, the oxidation of coexisting Fe^{2+} also contributes to the formation of these ROS through the photo-Fenton reaction. Among these ROS, •OH plays a critical role in the oxidation of As(III), and the generation of schwertmannite from the oxidation of a small amount of Fe^{2+} by •OH further leads to the adsorption and immobilization of As(T). In our previous work, As can be adsorbed on

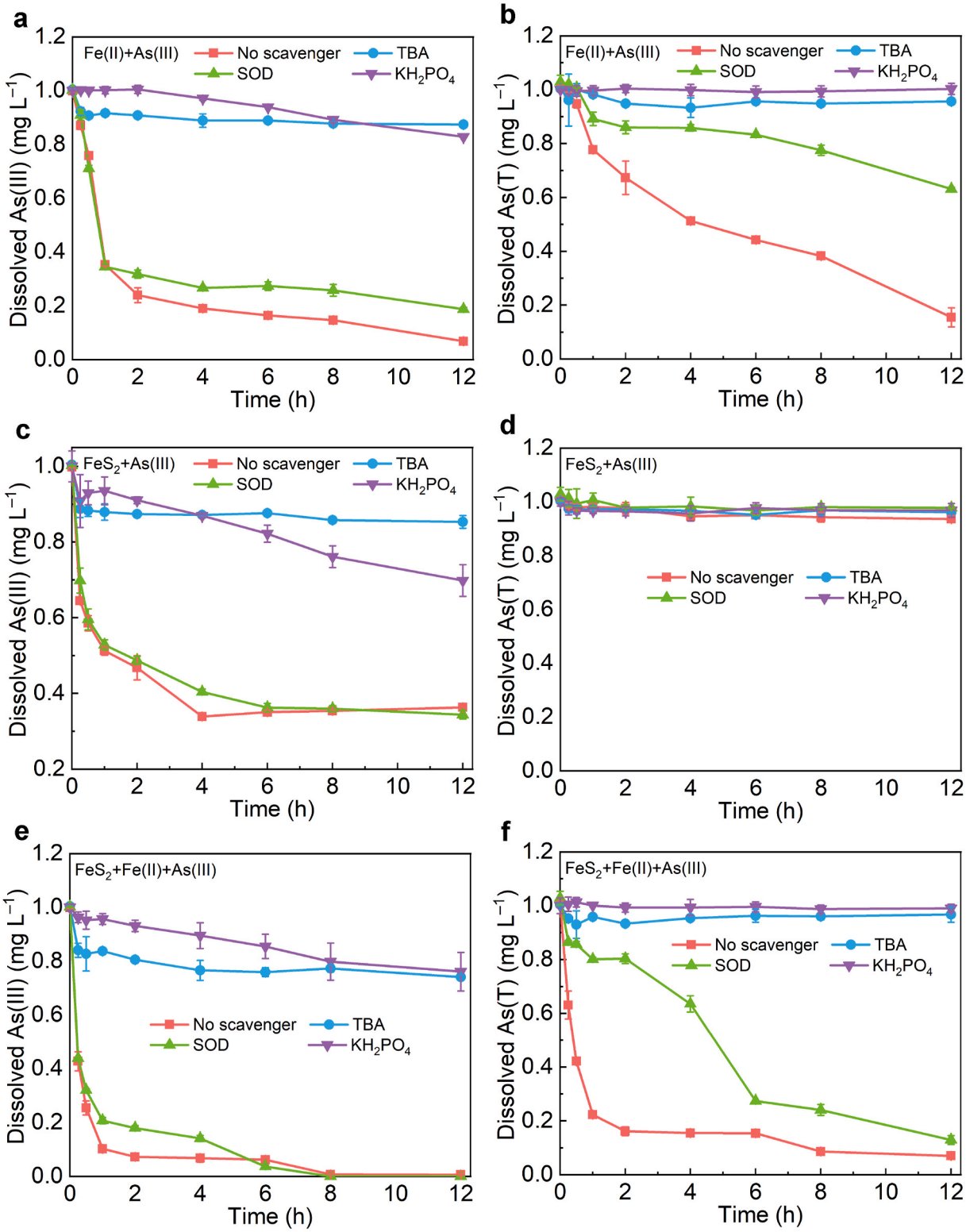

Fig. 6. Effect of scavengers on dissolved As(III) (a, c, e) and As(T) (b, d, f) in different reactions in air at initial pH 3.0. Initial concentration: $[pyrite]_0 = 0.75$ g L^{-1}, $[Fe^{2+}]_0 = 56.08$ mg L^{-1}, $[As(III)]_0 = 1.0$ mg L^{-1}, $[TBA]_0 = 200$ mmol L^{-1}, $[SOD]_0 = 25$ mg L^{-1} and $[KH_2PO_4]_0 = 10$ mmol L^{-1}.

pyrite and newly formed ferrihydrite in circumneutral environments under UV radiation (Liu et al., 2021), while no obvious adsorption of As (III) and As(V) was observed at pH 3.0 under dark and UV radiation in the absence of $FeSO_4$ in this work. As(III) mainly exists as H_3AsO_3 with pH 3–9, and As(V) is mainly present as $H_2AsO_4^-$ at pH 3–7 and $HAsO_4^{2-}$ at pH 7–9 (Liu et al., 2019), which may lead to the low adsorption capacity of As at pH 3.0 and significant adsorption of As(V) on pyrite in circumneutral environments.

4.2. Influence of dissolved oxygen and pH

As the main electron acceptor for Fe(II) and As(III) oxidation, O_2

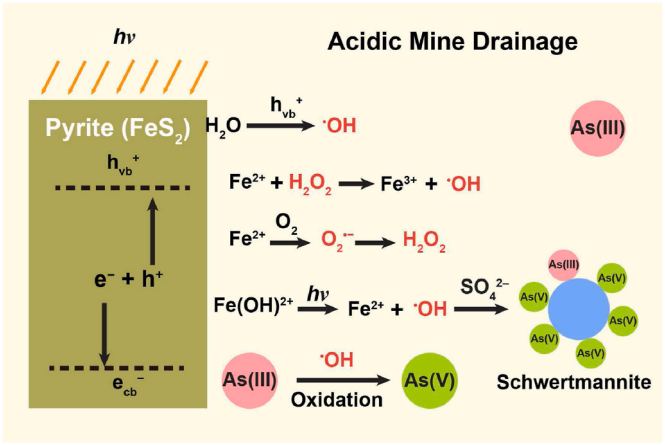

Fig. 7. Proposed reaction pathway for the photooxidation and immobilization of As(III) on pyrite under acidic conditions.

directly affects As(III) oxidation rate. As(III) oxidation still occurred in nitrogen, which might result from the production of •OH through the oxidation of water at the sulfur defect sites on pyrite and photo-Fenton reaction of Fe^{2+}/$Fe(OH)^{2+}$ (Qiu et al., 2017; Zhang et al., 2016). With the introduction of oxygen, the oxidation rate of As(III) sharply increased. The increase in dissolved oxygen concentration promoted •OH formation through the oxidation of pyrite (Eqs. 4–6 in Table S1) (Qiu et al., 2017). Moreover, the oxidation rate of Fe^{2+} to Fe(III) by air is slow in acidic environments. The increase in dissolved oxygen concentration enhanced the oxidation of Fe^{2+} to $Fe(OH)^{2+}$ and subsequently promoted the photo-Fenton reaction. Therefore, the improved oxidation and immobilization of As(III) can be mainly ascribed to the generation of more ROS including •OH and H_2O_2 and the oxidation of more Fe^{2+} in air and oxygen.

The rate of As(III) oxidation and immobilization rose when the initial pH increased within 2.0–4.0. The existing forms of Fe ions and the formation pathways of ROS vary with pH, affecting As(III) oxidation and immobilization. The oxidation rate of Fe^{2+} to Fe(III) increases with increasing pH (Liu et al., 2018). At pH 2.0 and 3.0, Fe(III) mainly exists as $Fe(OH)^{2+}$ and Fe^{3+} (Fig. S8), whose proportion increases and decreases with increasing pH, respectively (Kong et al., 2016). The increase in photo-Fenton reaction would lead to the oxidation of more As (III). When the pH was increased to 4.0, the proportion of $Fe(OH)^{2+}$ decreased and Fe(III) mainly existed as colloid ferric hydroxide (Kong et al., 2016). As reported, Sb(III)/As(III) could be adsorbed on colloid ferric hydroxide to form complexes, and electron transfer occurs from Sb (III)/As(III) to colloid ferric hydroxide, resulting in Sb(III)/As(III) oxidation under light radiation (Kong et al., 2016; Xu et al., 2014). Electron transfer from ligands to metals was also observed between Fe (II) and ferrihydrite under sunlight radiation in our previous work (Shu et al., 2019). Therefore, As(III) oxidation and immobilization increase with increasing pH.

Due to the significant environmental risks of acid mine wastewater, its treatment has always been a concern in the field of environment. Recently, some iron oxide-based on-site remediation techniques (such as entrapment with coastal sand, demolition wastes and biochar) have been developed for the stabilization of As in AMD, soil and sediments (Karna et al., 2017; Lee et al., 2021; Pat-Espadas et al., 2018). The results of this work indicate that sunlight radiation can promote the oxidation and immobilization of As(III) in AMD environments. Therefore, during the stabilization treatment of As(III) in actual AMD via these iron oxide-based stabilization techniques, sunlight radiation may significantly improve the stabilization efficiency of As(III).

5. Conclusions

Sunlight radiation significantly enhances As(III) oxidation and immobilization on pyrite under acidic conditions. Under light radiation, the h^+_{vb}–e^-_{cb} pairs formed on pyrite interact with oxygen and water to produce $O_2^{\bullet-}$, •OH and H_2O_2, and the photo-Fenton reaction of Fe $(OH)^{2+}$ formed from Fe^{2+} oxidation also leads to the formation of •OH. These ROS, particularly •OH, can enhance As(III) oxidation. The schwertmannite formed from the oxidation of a small amount of Fe^{2+} by •OH contributes to As adsorption and immobilization. The increase in dissolved oxygen concentration results in the production of more ROS and the oxidation of more Fe^{2+}, thereby enhancing As(III) oxidation and immobilization. The increase in pH also promotes As(III) oxidation and immobilization. At pH 2.0 and 3.0, As(III) is mainly oxidized by the •OH produced from the photo-Fenton reaction. At pH 4.0, Fe(III) formed from Fe^{2+} oxidation exists as colloidal iron hydroxide. As(III)-colloidal iron hydroxide complexes may undergo electron transfer from As(III) to colloidal iron hydroxide under light radiation, resulting in As(III) oxidation. The present work provides important insights into the environmental behavior of As in AMD. However, further investigation on the transformation and migration of As in actual AMD environments under sunlight should be performed, which will facilitate a better understanding of the geochemical cycling of As.

Credit author statement

Lihu Liu: Conceptualization, Methodology, Investigation, Writing – original draft. **Diman Guo**: Investigation, Methodology. **Guohong Qiu**: Writing – review & editing, Funding acquisition, Supervision. **Chengshuai Liu**: Writing – review & editing, Funding acquisition. **Zengping Ning**: Writing – review & editing, Resources, Funding acquisition, Supervision.

Declaration of competing interest

The authors declare that they have no known competing financial interests or personal relationships that could have appeared to influence the work reported in this paper.

Acknowledgments

This work was supported by the National Natural Science Foundation of China (Nos. 41877025, 42077133 and U21A2034), the National Key Research & Development Program of China (No. 2020YFC1808503), West Light Foundation and the Frontier Science Research Programme of the Chinese Academy of Sciences (No. QYZDB-SSW-DQC046), Leading Talent of "Ten Thousand Plan"-National High-Level Talents Special Support Plan and the Natural Science Foundation of Hubei Province of China (No. 2020CFA013). We are grateful to Dr. Lihong Qin (Public Laboratory of Electron Microscope of Huazhong Agricultural University) for assistance with characterization of SEM. This work was carried out with the support of 1W1B beamline at Beijing Synchrotron Radiation Facility. The authors also owe thank Limei Zhang, Huan He and Shu Zhu at the public laboratory platform of the College of Resources and Environment, Huazhong Agricultural University, for their help with experimental test.

Appendix A. Supplementary data

Supplementary data to this article can be found online at https://doi.org/10.1016/j.jenvman.2022.115425.

References

Ahmad, A., van der Wens, P., Baken, K., de Waal, L., Bhattacharya, P., Stuyfzand, P., 2020. Arsenic reduction to < 1 μg/L in Dutch drinking water. Environ. Int. 134, 105253. https://doi.org/10.1016/j.envint.2019.105253.

Alonso, D.L., Perez, R., Okio, C., Castillo, E., 2020. Assessment of mining activity on arsenic contamination in surface water and sediments in southwestern area of Santurban paramo, Colombia. J. Environ. Manag. 264, 110478. https://doi.org/10.1016/j.jenvman.2020.110478.

Asif, M.B., Price, W.E., Fida, Z., Tufail, A., Ren, T., Hai, F.I., 2021. Acid mine drainage and sewage impacted groundwater treatment by membrane distillation: organic micropollutant and metal removal and membrane fouling. J. Environ. Manag. 291, 112708. https://doi.org/10.1016/j.jenvman.2021.112708.

Aydin, G., 2014. The modeling of coal-related CO_2 emissions and projections into future planning. Energy Sources, Part A 36, 191–201. https://doi.org/10.1080/15567036.2012.760018.

Aydin, G., Karakurt, I., Aydiner, K., 2012. Analysis and mitigation opportunities of methane emissions from the energy sector. Energy Sources, Part A 34, 967–982. https://doi.org/10.1080/15567031003716725.

Bhandari, N., Reeder, R.J., Strongin, D.R., 2011. Photoinduced oxidation of arsenite to arsenate on ferrihydrite. Environ. Sci. Technol. 45, 2783–2789. https://doi.org/10.1021/es103793y.

Bhandari, N., Reeder, R.J., Strongin, D.R., 2012. Photoinduced oxidation of arsenite to arsenate in the presence of goethite. Environ. Sci. Technol. 46, 8044–8051. https://doi.org/10.1021/es300988p.

Chandra, A.P., Gerson, A.R., 2011. Pyrite (FeS_2) oxidation: a sub-micron synchrotron investigation of the initial steps. Geochem. Cosmochim. Acta 75, 6239–6254. https://doi.org/10.1016/j.gca.2011.08.005.

Diao, Z., Shi, T., Wang, S., Huang, X., Zhang, T., Tang, Y., Zhang, X., Qiu, R., 2013. Silane-based coatings on the pyrite for remediation of acid mine drainage. Water Res. 47, 4391–4402. https://doi.org/10.1016/j.watres.2013.05.006.

Ding, W., Xu, J., Chen, T., Liu, C., Li, J., Wu, F., 2018. Co-oxidation of As(III) and Fe(II) by oxygen through complexation between As(III) and Fe(II)/Fe(III) species. Water Res. 143, 599–607. https://doi.org/10.1016/j.watres.2018.06.072.

Doane, T.A., 2017. A survey of photogeochemistry. Geochem. Trans. 18, 1–24. https://doi.org/10.1186/s12932-017-0039-y.

Ferreira, P.M., Majuste, D., Freitas, E.T.F., Caldeira, C.L., Dantas, M.S.S., Ciminelli, V.S. T., 2021. Galvanic effect of pyrite on arsenic release from arsenopyrite dissolution in oxygen-depleted and oxygen-saturated circumneutral solutions. J. Hazard Mater. 412, 125236. https://doi.org/10.1016/j.jhazmat.2021.125236.

Fu, D., Kurniawan, T.A., Lin, L., Li, Y., Avtar, R., Dzarfan Othman, M.H., Li, F., 2021. Arsenic removal in aqueous solutions using FeS_2. J. Environ. Manag. 286, 112246. https://doi.org/10.1016/j.jenvman.2021.112246.

Gabarron, M., Faz, A., Martinez-Martinez, S., Acosta, J.A., 2018. Change in metals and arsenic distribution in soil and their bioavailability beside old tailing ponds. J. Environ. Manag. 212, 292–300. https://doi.org/10.1016/j.jenvman.2018.02.010.

Georgiou, C.D., Sun, H.J., McKay, C.P., Grintzalis, K., Papapostolou, I., Zisimopoulos, D., Panagiotidis, K., Zhang, G., Koutsopoulou, E., Christidis, G.E., Margiolaki, I., 2015. Evidence for photochemical production of reactive oxygen species in desert soils. Nat. Commun. 6, 7100. https://doi.org/10.1038/ncomms8100.

Han, G., Wen, S., Wang, H., Feng, Q., 2020. Selective adsorption mechanism of salicylic acid on pyrite surfaces and its application in flotation separation of chalcopyrite from pyrite. Separ. Purif. Technol. 240, 116650. https://doi.org/10.1016/j.seppur.2020.116650.

Hong, J., Liu, L., Luo, Y., Tan, W., Qiu, G., Liu, F., 2018. Photochemical oxidation and dissolution of arsenopyrite in acidic solutions. Geochem. Cosmochim. Acta 239, 173–185. https://doi.org/10.1016/j.gca.2018.07.034.

Hong, J., Liu, L., Ning, Z., Liu, C., Qiu, G., 2021. Synergistic oxidation of dissolved As(III) and arsenopyrite in the presence of oxygen: formation and function of reactive oxygen species. Water Res. 202, 117416. https://doi.org/10.1016/j.watres.2021.117416.

Hong, J., Liu, L., Tan, W., Qiu, G., 2020. Arsenic release from arsenopyrite oxidative dissolution in the presence of citrate under UV irradiation. Sci. Total Environ. 726, 138429. https://doi.org/10.1016/j.scitotenv.2020.138429.

Hu, X., Kong, L., He, M., 2014. Kinetics and mechanism of photopromoted oxidative dissolution of antimony trioxide. Environ. Sci. Technol. 48, 14266–14272. https://doi.org/10.1021/es503245v.

Joo, S.H., Feitz, A.J., Sedlak, D.L., Waite, T.D., 2005. Quantification of the oxidizing capacity of nanoparticulate zero-valent iron. Environ. Sci. Technol. 39, 1263–1268. https://doi.org/10.1021/es048983d.

Karna, R.R., Luxton, T., Bronstein, K.E., Redmon, J.H., Scheckel, K.G., 2017. State of the science review: potential for beneficial use of waste by-products for in situ remediation of metal-contaminated soil and sediment. Crit. Rev. Environ. Sci. Technol. 47, 65–129. https://doi.org/10.1080/10643389.2016.1275417.

Kim, E.J., Batchelor, B., 2009. Macroscopic and X-ray photoelectron spectroscopic investigation of interactions of arsenic with synthesized pyrite. Environ. Sci. Technol. 43, 2899–2904. https://doi.org/10.1021/es803114g.

Koley, S., 2021. Future perspectives and mitigation strategies towards groundwater arsenic contamination in West Bengal, India. Environ. Qual. Manag. 1–23 https://doi.org/10.1002/tqem.21784.

Köne, A.Ç., Büke, T., 2010. Forecasting of CO_2 emissions from fuel combustion using trend analysis. Renew. Sustain. Energy Rev. 14, 2906–2915. https://doi.org/10.1016/j.rser.2010.06.006.

Kong, L., He, M., Hu, X., 2016. Rapid photooxidation of Sb(III) in the presence of different Fe(III) species. Geochem. Cosmochim. Acta 180, 214–226. https://doi.org/10.1016/j.gca.2016.02.022.

Kong, L., Hu, X., He, M., 2015. Mechanisms of Sb(III) oxidation by pyrite-induced hydroxyl radicals and hydrogen peroxide. Environ. Sci. Technol. 49, 3499–3505. https://doi.org/10.1021/es505584r.

Le Pape, P., Blanchard, M., Brest, J., Boulliard, J.C., Ikogou, M., Stetten, L., Wang, S., Landrot, G., Morin, G., 2017. Arsenic incorporation in pyrite at ambient temperature at both tetrahedral S^{-1} and octahedral Fe^{II} sites: evidence from EXAFS-DFT analysis. Environ. Sci. Technol. 51, 150–158. https://doi.org/10.1021/acs.est.6b03502.

Lee, H., Choi, W., 2002. Photocatalytic oxidation of arsenite in TiO_2 suspension: kinetics and mechanisms. Environ. Sci. Technol. 36, 3872–3878. https://doi.org/10.1021/es0158197.

Lee, Y., Cui, M., Son, Y., Ma, J., Han, Z., Khim, J., 2021. Evaluation of stabilizing material and stabilization efficiency through comparative study of toxic heavy metal transfer between corn and peanut grown in stabilized field soil. Environ. Pollut. 275, 116617. https://doi.org/10.1016/j.envpol.2021.116617.

Liu, L., Chen, H., Yang, X., Tan, W., Liu, C., Dang, Z., Qiu, G., 2020. High-efficiency As (III) oxidation and electrocoagulation removal using hematite with a charge-discharge technique. Sci. Total Environ. 703, 135678. https://doi.org/10.1016/j.scitotenv.2019.135678.

Liu, L., Guo, D., Ning, Z., Liu, C., Qiu, G., 2021. Solar irradiation induced oxidation and adsorption of arsenite on natural pyrite. Water Res. 203, 117545. https://doi.org/10.1016/j.watres.2021.117545.

Liu, L., Jia, Z., Tan, W., Suib, S.L., Ge, L., Qiu, G., Hu, R., 2018. Abiotic photomineralization and transformation of iron oxide nanominerals in aqueous systems. Environ. Sci.: Nano 5, 1169–1178. https://doi.org/10.1039/c7en01242j.

Liu, L., Tan, W., Suib, S.L., Qiu, G., Zheng, L., Su, S., 2019. Enhanced adsorption removal of arsenic from mining wastewater using birnessite under electrochemical redox reactions. Chem. Eng. J. 375, 122051. https://doi.org/10.1016/j.cej.2019.122051.

Lu, A., Li, Y., Ding, H., Xu, X., Li, Y., Ren, G., Liang, J., Liu, Y., Hong, H., Chen, N., Chu, S., Liu, F., Li, Y., Wang, H., Ding, C., Wang, C., Lai, Y., Liu, J., Dick, J., Liu, K., Hochella Jr., M.F., 2019. Photoelectric conversion on Earth's surface via widespread Fe- and Mn-mineral coatings. Proc. Natl. Acad. Sci. U. S. A. 116, 9741–9746. https://doi.org/10.1073/pnas.1902473116.

Majzlan, J., Alpers, C.N., Koch, C.B., McCleskey, R.B., Myneni, S.C.B., Neil, J.M., 2011. Vibrational, X-ray absorption, and Mössbauer spectra of sulfate minerals from the weathered massive sulfide deposit at Iron Mountain, California. Chem. Geol. 284, 296–305. https://doi.org/10.1016/j.chemgeo.2011.03.008.

Park, I., Ryota, T., Yuto, T., Tabelin, C.B., Phengsaart, T., Jeon, S., Ito, M., Hiroyoshi, N., 2021. A novel arsenic immobilization strategy via a two-step process: arsenic concentration from dilute solution using schwertmannite and immobilization in Ca-Fe-AsO_4 compounds. J. Environ. Manag. 295, 113052. https://doi.org/10.1016/j.jenvman.2021.113052.

Pat-Espadas, A., Loredo Portales, R., Amabilis-Sosa, L., Gómez, G., Vidal, G., 2018. Review of constructed wetlands for acid mine drainage treatment. Water 10, 1685. https://doi.org/10.3390/w10111685.

Podgorski, J., Berg, M., 2020. Global threat of arsenic in groundwater. Science 368, 845–850. https://doi.org/10.1126/science.aba1510.

Qiu, G., Gao, T., Hong, J., Luo, Y., Liu, L., Tan, W., Liu, F., 2018. Mechanisms of interaction between arsenian pyrite and aqueous arsenite under anoxic and oxic conditions. Geochem. Cosmochim. Acta 228, 205–219. https://doi.org/10.1016/j.gca.2018.02.051.

Qiu, G., Gao, T., Hong, J., Tan, W., Liu, F., Zheng, L., 2017. Mechanisms of arsenic-containing pyrite oxidation by aqueous arsenate under anoxic conditions. Geochem. Cosmochim. Acta 217, 306–319. https://doi.org/10.1016/j.gca.2017.08.030.

Shu, Z., Liu, L., Tan, W., Suib, S.L., Qiu, G., Yang, X., Zheng, L., Liu, F., 2019. Solar irradiation induced transformation of ferrihydrite in the presence of aqueous Fe^{2+}. Environ. Sci. Technol. 53, 8854–8861. https://doi.org/10.1021/acs.est.9b02750.

Tabelin, C.B., Corpuz, R.D., Igarashi, T., Villacorte-Tabelin, M., Alorro, R.D., Yoo, K., Raval, S., Ito, M., Hiroyoshi, N., 2020. Acid mine drainage formation and arsenic mobility under strongly acidic conditions: importance of soluble phases, iron oxyhydroxides/oxides and nature of oxidation layer on pyrite. J. Hazard Mater. 399, 122844. https://doi.org/10.1016/j.jhazmat.2020.122844.

Tamura, H., Goto, K., Yotsuyanagi, T., Nagayama, M., 1974. Spectrophotometric determination of iron(II) with 1,10-phenanthroline in the presence of large amounts of iron(III). Talanta 21, 314–318. https://doi.org/10.1016/0039-9140(74)80012-3.

Wang, C., Liu, R., Ahmed Khoso, S., Lu, H., Sun, W., Ni, Z., Lyu, F., 2020. Combined inhibitory effect of calcium hypochlorite and dextrin on flotation behavior of pyrite and galena sulphides. Miner. Eng. 150, 106274. https://doi.org/10.1016/j.mineng.2020.106274.

Wang, X., Ying, H., Zhao, W., Feng, X., Tan, W., Beyer, K.A., Huang, Q., Liu, F., Zhu, M., 2021. Molecular-Scale understanding of sulfate exchange from schwertmannite by chromate versus arsenate. Environ. Sci. Technol. 55, 5857–5867. https://doi.org/10.1021/acs.est.0c07980.

Xu, J., Li, J., Wu, F., Zhang, Y., 2014. Rapid photooxidation of As(III) through surface complexation with nascent colloidal ferric hydroxide. Environ. Sci. Technol. 48, 272–278. https://doi.org/10.1021/es403667b.

Xu, Z., Wan, Z., Sun, Y., Cao, X., Hou, D., Alessi, D.S., Ok, Y.S., Tsang, D.C.W., 2021. Unraveling iron speciation on Fe-biochar with distinct arsenic removal mechanisms and depth distributions of as and Fe. Chem. Eng. J. 425, 131489. https://doi.org/10.1016/j.cej.2021.131489.

Yu, Y., Zhu, Y., Gao, Z., Gammons, C.H., Li, D., 2007. Rates of arsenopyrite oxidation by oxygen and Fe(III) at pH 1.8–12.6 and 15–45 °C. Environ. Sci. Technol. 41, 6460–6464. https://doi.org/10.1021/es070788m.

Zhang, H., Chen, G., Cai, X., Fu, J., Liu, M., Zhang, P., Yu, H., 2021. The leaching behavior of copper and iron recovery from reduction roasting pyrite cinder. J. Hazard Mater. 420, 126561. https://doi.org/10.1016/j.jhazmat.2021.126561.

Zhang, P., Yuan, S., Liao, P., 2016. Mechanisms of hydroxyl radical production from abiotic oxidation of pyrite under acidic conditions. Geochem. Cosmochim. Acta 172, 444–457. https://doi.org/10.1016/j.gca.2015.10.015.

Zhong, D., Zhao, Z., Jiang, Y., Yang, X., Wang, L., Chen, J., Guan, C.Y., Zhang, Y., Tsang, D.C.W., Crittenden, J.C., 2020. Contrasting abiotic As(III) immobilization by undissolved and dissolved fractions of biochar in Ca^{2+}-rich groundwater under anoxic conditions. Water Res. 183, 116106. https://doi.org/10.1016/j.watres.2020.116106.